UC Office of the President

Recent Work

Title

Applications of Dynamic Contrast Enhanced MRI in Oncology: Measurement of Tumor Oxygen Tension

Permalink

https://escholarship.org/uc/item/06r5d7kb

Authors

Wang, Z.
Su, M-Y
Nalcioglu, O.

Publication Date

2002-02-01

DOI

10.1177/153303460200100104

Peer reviewed

Applications of Dynamic Contrast Enhanced MRI in Oncology: Measurement of Tumor Oxygen Tension

www.tcrt.org

Z. Wang, Ph.D.
M-Y. Su, Ph.D.
O. Nalcioglu, Ph.D.*

John Tu and Thomas Yuen

Center for Functional Onco-Imaging

College of Medicine

University of California

Irvine, CA 92697-5020, USA

A new model based on an extension of the Krogh's cylindrical model was developed to calculate tumor oxygen tension (pO_2) from the H-1 dynamic contrast enhanced MRI (DCE-MRI) measurements. The model enables one to calculate the tumor pO_2 using the vascular volume fraction (f_b) obtained by the DCE-MRI. The proposed model has three parameters. For small values of f_b one assumes that there exists a linear relationship between and f_b. The constant of proportionality in this case is given by C_1 - the oxygen tension per vascular volume fraction. For larger values of f_b a modified version of Krogh model using two parameters is developed and here C_2 - is the integrated blood oxygen tension, and C_3 - given by the combination of the oxygen diffusion coefficient, solubility of oxygen in the tissue, capillary radius, and tissue metabolic consumption rate. The parameters of the model can be determined by performing simultaneous in-vivo F-19 MRI oxygen tension measurement and dynamic Gd-DTPA enhanced MRI on the same tumor. Dynamic MRI data can be used with a compartmental model to calculate tumor vascular volume fraction on a pixel by pixel basis. Then tumor oxygen tension map can be calculated from the vascular volume fraction by the extended Krogh model as described above. In the present work, the model parameters were determined using three rats bearing Walker-256 tumors and performing simultaneous F-19 and DCE MRI on the same tumor. The parameters obtained by fitting the model equation to the experimental data were: C_1 = 983.2$\pm$ 133.2torr, C_2 = 58.20 $\pm$ 2.4 torr, and C_3 = 1.7 $\pm$ 0.1 torr. The performance of the extended Krogh model was then tested on two additional rats by performing both F-19 and DCE-MRI studies and calculating the pO_2 (H-1) using the model and comparing it with the pO_2 (F-19) obtained from the F-19 MRI. It was found that the measurements obtained by both techniques had a high degree of correlation [pO_2 (H-1) = (1.01 $\pm$ 0.07) pO_2 (F-19) + (0.91 $\pm$ 0.05) and r=0.96], indicating the applicability of the proposed model in determining pO_2 from the DCE-MRI.

Introduction

Tumor oxygenation has long been recognized as an important factor for radiosensitivity and become a major determinant in predicting the outcome of radiotherapy (1-4). The reason for this being that the ratio of the radiation dose needed to achieve the same biological effect for anoxic and aerated tumor cells is generally between 2.5 - 3 for therapeutic photon beams (5). In the past, the oxygen electrode method (6-9) has been used to measure tumor oxygenation, yet it is invasive and a non-imaging modality. Furthermore, it only provides oxygenation information within a region of about 200 mm around the tip of the electrode, while the oxygenation within a tumor could be very heterogeneous due to the existence of the highly vascular areas, the poorly vascular hypoxic regions and the necrotic sections (10, 11). Although this could be circumvented by using additional electrodes the problem of inadequate spatial sampling usually remains. Thus, there is a great need to develop a tumor oxygenation mapping technique that can easily be implemented in a clinical setting and also provide

*Corresponding author:
O. Nalcioglu, Ph.D.
E-mail: nalci@uci.edu

spatially resolved measurements throughout the tumor.

F-19 MRI has recently been used for tumor oxygen tension mapping (12-19). The spin-lattice relaxation rate of perfluorocarbon (PFC) emulsions has a linear relation with the dissolved oxygen concentration. Hence tissue oxygen tension maps can be obtained by measuring the relaxation rate of the tissue-sequestered perfluorocarbon using F-19 MRI. A great amount of effort has been put in the past to overcome the technical difficulties associated with F-19 imaging including the chemical shift artifacts due to the multiple resonance peaks that exist in many perfluorocarbon emulsions (20-30). In order to solve this problem, Dardzinski and Sotak (17) developed F-19 MRI using a single peak perfluorocarbon named perfluoro-15-crown-5-ether. Recently, dynamic Gd-DTPA enhanced MRI (DCE-MRI) has been applied extensively to study tumors (31-33). It has been shown that with proper compartmental modeling (34-42) one can separate the tracer concentration within intravascular space from the one within interstitial space. This yields valuable data on tumor vascular volume fraction that is closely related to the tumor oxygen supply.

Theory

The cylindrical model was first introduced by Krogh (43) to calculate the oxygen tension within a tissue cylinder with a concentric capillary in the center. Considering the mass balance between the oxygen consumption and supply, which arises from oxygen diffusion in the tissue, the tissue oxygen tension distribution along the radial direction within the tissue cylinder can be described by the following differential equation:

$$D \frac{1}{r} \frac{d}{dr} \left(r \frac{dP}{dr} \right) - \frac{m}{S^T} = 0 \qquad [1]$$

where P(r) is the tissue oxygen tension at a radial distance r from the central axis of the cylinder, D is the oxygen diffusion coefficient, m is the tissue metabolic consumption rate, and ST is the solubility of oxygen in the tissue. After integrating Eq. [1], the oxygen tension distribution within the Krogh's cylinder can be expressed as (44):

$$P = P_0 - \frac{mR_2^2}{2DS^T} \ln \frac{r}{R_1} - \frac{mR_1^2}{4DS^T} \left(1 - \frac{r^2}{R_1^2} \right) \qquad [2]$$

where R_1 is the capillary radius, R_2 is the radius of the Krogh's cylinder, P = P(r) and P_0 is the oxygen tension at the vessel walls. Equation [2] describes the dependence of tissue oxygen tension P on the radial distance r within the cylinder with $R_1 \le r \le R_2$. In order to relate the data obtained from the F-19 MRI oxygen tension mapping to the dynamic contrast enhanced MRI vascular volume fraction imaging, we must further integrate the oxygen tension within the Krogh's cylinder and convert

R_1^2/R_2^2 to the vascular volume fraction fb. After integrating equation [2] over "r" the relationship between the oxygen tension and the vascular volume fraction, both averaged over a voxel, is given by:

$$pO_2 = C_2 + C_3 \left[\frac{\ln f_b}{4(f_b - f_b^2)} + \frac{3}{8 f_b} - \frac{1}{8} \right] \qquad [3]$$

where $C_2 = \overline{P_O}$ is the average oxygen tension integrated along the vessel walls and $C_3 = mR_1^2/DS^T$ is a parameter combining the oxygen diffusion coefficient, solubility of oxygen in the tissue, capillary radius, and tissue metabolic consumption rate.

It should be noted that equation [3] becomes singular when f_b approaches to zero. In order to extrapolate this equation to low pO_2 values, which are more interesting biologically, we further assume that in this region the pO_2 is linearly proportional to f_b, that is,

$$pO_2 = C_1 f_b \qquad [4]$$

This assumption is reasonable especially when the oxygen diffusion from blood is the only source of oxygen supply in tissue. The constant C_1 is determined by choosing this straight line to be tangent to the curve given by equation [3]. Equations (3) and (4) define the extended Krogh model that is applicable at all pO_2 values.

By using the pO_2 values obtained from the F-19 MRI and f_b values by the dynamic Gd-DTPA enhanced MRI, the parameters C_1, C_2 and C_3 can be determined by a least squares fitting of Eqs. (3-4). After C_1, C_2 and C_3 are obtained, one can calculate the tumor oxygen tension map from the vascular volume fraction values derived from the H-1 dynamic contrast enhanced MRI alone using Eqs. [3-4].

Materials and Methods

Tumor Model and MRI Experiments

Five female Sprague Dawley rats were implanted with Walker 256 tumors in the thighs. About 10^7 tumor cells were injected intramuscularly to grow a tumor. The tumor cells were harvested from donor rats and preserved in RPMI 1640 (49). These tumors grew slowly in the first three days and much faster later. On the sixth day after the implantation, the tumor grew to a size of about 2 cm in diameter with some necrotic region present in the center. The rats were anesthetized with 50 mg/kg Ketamine plus 5 mg/kg Rompun and surrounded by foam to maintain a constant body temperature during the MRI scans. The temperature of each animal was monitored throughout the experiment and was found to be 37.0 ± 1.0 ºC averaged over five animals. The animals were breathing room air during the MR studies. All the MRI experiments were performed using a 1.5T whole body magnet with the SMIS (Surrey Medical Imaging Systems, UK) data acquisition system. A home made double-tuned RF coil was used to acquire both the F-19 and H-1 images of the

same slice. Perfluoro-15-crown-5-ether emulsion (40% v/v, HemaGen, St. Louis, MO), which resonates at a single frequency was used to avoid the chemical shift artifacts (17). One c.c. of the emulsion was slowly injected into the tumor during several minutes one hour before the measurement using a 28-gauge needle. The needle was placed at 3 - 5 positions along an off-center line with the deepest position being the first. An H-1 multi-slice T_2 weighted SE pulse sequence with TR / TE = 1500 ms / 110 ms was used to localize and acquire anatomical axial slices of the tumor region. A set of six spin echo F-19 images with different TR values (1, 1.5, 2, 2.5, 3 and 5 seconds) were used to measure the R_1 for the calculation of tumor oxygen tension. The image slices were prescribed through both tumor and liver regions. The other imaging parameters for F-19 imaging were: TE = 30 ms, FOV = 16 cm, matrix = 128 x 128, and slice thickness = 5 mm. Right after collecting the F-19 images for each rat, a series of 45 sets of dynamic Gd-DTPA enhanced short-TR spin echo images were acquired with a temporal resolution of 18.8 seconds on the same slices as in the case of F-19 MRI. For both imaging techniques two slices were selected through the tumor while one was through the liver. The liver slice in the DCE-MRI was used for calibration as discussed above while the F-19 and H1 pO_2 studies were confined to the two slices passing through the tumor. The imaging parameters were the same as the F-19 images except that TR / TE = 133.3 msec / 10 msec. A bolus of Gd-DTPA (Magnevist, Berlex) at a dose of 0.1 mmol/kg was injected at the beginning of the 5th image. We performed both the F-19 and H-1 dynamic Gd-DTPA enhanced MRI on five rats bearing Walker 256 tumors. The parameters C_1, C_2, and C_3 in Eqs. (3-4) were obtained by fitting the (F-19) obtained from F-19 imaging and f_b (H-1) calculated from the dynamic enhanced MRI data on the first three rats. In order to assure that there was no slice shift between the F-19 and H-1 images, we first placed half a bottle of perfluoro-15-crown-5-ether emulsion obliquely within the coil and repeated the F-19 and H-1 MRI measurements. We then subtracted the F-19 and H-1 images to check the slice shift in the x, y and z directions. No shift of slice position was observed in any of the three directions.

Calculation of pO$_2$ Values from the F-19 MRI

Using the sets of F-19 images acquired at various TR's, we found all the tumor pixels that contained perfluoro-15-crown-5-ether emulsion and performed pixel wise nonlinear least squares fitting according to $S=S_0(1-e^{-TR \cdot R_1})$ to measure the R_1 value for each pixel. The R_1 values were converted to oxygen tension values through a calibration curve. The calibration curve between R_1 and oxygen tension was obtained by measuring the R_1 values of a phantom with various oxygenation states at 37 °C, which was controlled by a water bath.

Two needles were inserted through the rubber seal for bubbling. The longer needle was pushed to the bottom and used as inlet of the bubbling gas. The shorter needle was above the surface and used as the outlet of the bubbling gas. The phantom was bubbled with 0, 9.5%, 21% and 100% oxygen with a balance of nitrogen for 30 minutes to reach an equilibrium of oxygen tension. The signal intensities for six different TR values were read from the magnitude of the FID signal. Five independent readings were obtained for each TR. The calibration equation was obtained by a linear least squares fitting of the R_1 at various oxygen tension values under the assumption that R_1 and pO_2 are linearly related (50).

Calculation of Vascular Volume Fractions

The dynamic Gd-DTPA enhanced MRI signal time course was analyzed by the two-compartment model as described by Tofts (43) to extract the vascular fraction values. In this model, the tracer concentration in a tumor tissue voxel is assumed to be composed of the intravascular and the extravascular contributions. Then the time evolution of the tracer concentration can be described by the following equation:

$$C_t(t) = k_{in}^{PS\rho} \int_0^t C_p(t') e^{-\left(k_{out}^{PS\rho}/v_e\right)(t-t')} dt' + v_p C_p(t) \quad [5]$$

where C_t is the tracer concentration in the whole tumor tissue voxel, C_p is the plasma concentration, v_p is the plasma volume fraction, $K_{in}^{PS\rho}$ and $K_{out}^{PS\rho}$ are the apparent permeability values diffusing into and out of the extravascular-extracellular space and ve is the volume fraction of the extravascular-extracellular space. The first term represents the accumulation in the early stage and clearance in the late stage of the extravascular contribution, and the second term is due to the intravascular contribution. The tracer concentrations in tissue (C_t) and plasma (C_p) can be replaced by the Δ-signals of the tumor tissue and plasma as measured by the dynamic Gd-DTPA enhanced MRI by assuming the linearity between the concentration and the Δ-signal. The Δ-signal is defined to be the MRI signal intensity at time "t" minus the baseline signal before the contrast agent administration. This linearity holds if TR << T_1, which was satisfied by the pulse sequence used in the current investigation. The constant of proportionality as described in equation [24] of reference (43) for different tissues depends on their proton density, which is almost the same for various tissues. Therefore, the constant of proportionality can be eliminated from both sides of equation [5], and the concentrations can be simply replaced by the Δ-signals. In the present study the plasma signal was derived from the liver, which was used as the reference tissue. Since liver has non-continuous type of capillaries, Gd-DTPA molecules can quickly reach equilibrium and the kinetics of the compound within the liver tissue is similar to that in blood thus we
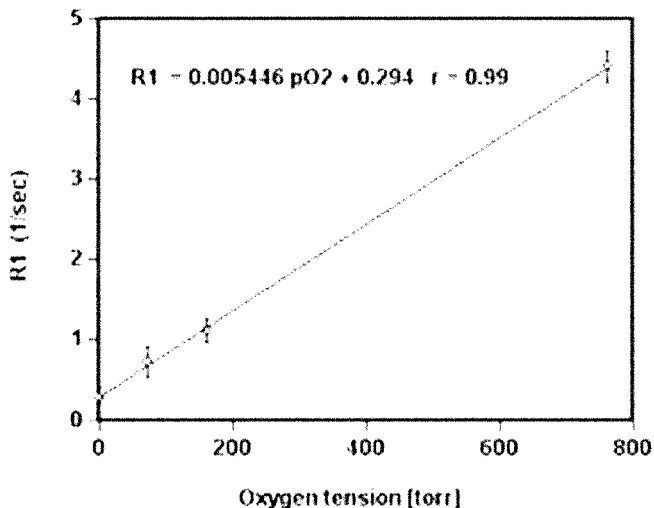
Figure 1: The calibration curve between the R1 values and oxygen tension. The error bars show the standard deviations. The fitted line was R1 (s-1) = (0.294 ± 0.008) + (0.005446 ± 0.00016) x (torr).

Figure 2: F-19 signal intensities at various TR's from a pixel with the fitted R1 value of 0.502 ± 0.015 s-1. This resulted in a value of 38.1 ± 2.8 torr from Eq. (6).

believe that this was a good choice. The liver Δ-signal was converted to the plasma Δ-signal by multiplying it with a scaling factor of 6.87, which is the inverse of the product of (1 - Hct) and the liver blood volume fraction 0.31 (45-48) where Hct is the fractional hematocrit. A nonlinear least squares fitting was performed for each tumor pixel to extract the values of v_p, $K_{in}^{PS\rho}$ and $K_{out}^{PS\rho}$/ve from the Δ-signal time course curve. The plasma volume fraction vp was converted to the whole vascular volume fraction using the factor 1/(1-Hct) = 2.13. The Δ-signal for tumor and liver were obtained by subtracting the baseline signal intensities of the images acquired before the injection of the contrast agents from those acquired after the injection.

Tumor Oxygen Tension Mapping from the H-1 Dynamic Gd-DTPA Enhanced MRI

The pO_2 (F-19) maps from the F-19 MRI and the corresponding vascular volume fraction (f_b) images from the dynamic Gd-DTPA enhanced MRI were generated for all the pixels containing perfluoro-15-crown-5-ether emulsion. Then a histogram of pixels according to their vascular volume fraction (f_b) value was formed going from low to high f_b. Pixels falling within a range of Df_b = 0.005 were averaged both in their f_b value as well as their corresponding pO_2 (F-19) values to improve the SNR. The process was repeated for all five animals individually. The data collected on the three rats was used to generate the pO_2 (F-19) vs. f_b (H-1) curve. The model constants C1, C2, and C3 were determined by a least squares fitting of equations [3-4] to the experimental data.

In order to test the performance of the model, the fitted pO_2 vs. f_b curve was used on the remaining two rats who also had both F-19 and DCE- MRI studies. The data collected on
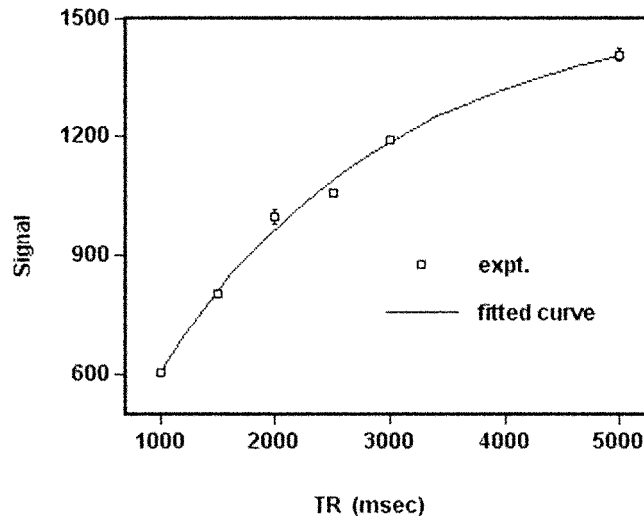
them was analyzed similar to the previous three rats. The f_b values obtained from the DCE-MRI study were substituted into equations [3-4], using the previously determined constants to calculate the pO_2 (H-1) pixel wise. These values were then compared with the pO_2 (F-19) measurements obtained by F-19 MRI from the corresponding regions.

Results

Oxygen Tension and R1 Calibration Curve

The calibration curve being used to convert the R1 values to the oxygen tension was measured at 0, 9.5, 21, and 100% O2 at 37 ºC. The R1 values were averaged over five FID measurements, and plotted in figure 1. The error bars show the standard deviation. The relation between R1 value and oxygen tension was obtained by linear least squares fitting, and given by:

$$R_1 \text{ (s}^{-1}) = n + m \text{ x } pO_2 \text{ (torr)} \qquad [6]$$

with a correlation coefficient of r = 0.99. The parameters of the fitting were n = 0.294 ± 0.008 and m = 0.005446 ± 0.00016.

Determination of the Extended Krogh Model Parameters

The pO_2 values for each pixel were calculated by using equation [6] and R1 values obtained using six different TR's in F-19 MRI. Figure 2 shows a typical set of signal intensities at various TR and a fitted curve by the nonlinear least squares fitting. The R1 value of this pixel was 0.502 + 0.015 s-1 and was converted to the pO_2 value of 38.2 ± 2.8 torr.

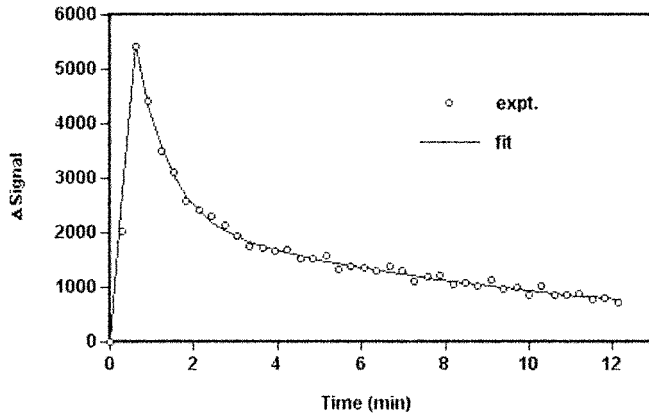The dynamic Gd-DTPA enhanced MRI signal time courses

Figure 3: The reference plasma D-signal time course that was obtained from a dynamic Gd-DTPA enhanced MRI on a liver slice of a rat and fitted by the nonlinear least squares to a bi-exponential decay curve given by , with A = 3,192 ± 128, a = 1.287 ± 0.051 min-1, B = 2,232 ± 67, and b = 0.0932 ± 0.0056 min-1.

Figure 4: The D-signal time course for a pixel and the compartmental modeling analysis with the fitting parameters were: vp = 0.0203 ± 0.0020 ml/g, = 0.0589 ± 0.0041 min-1 and /ve = 0.2440 ± 0.0146 min-1. The D-signal time evolution was separated into the extravascular (dotted line) and intravascular (dashed line) components corresponding to the first and the second terms in Eq. [5].

were analyzed by the two-compartment model according to equation [5]. The reference plasma Δ-signal time course obtained from the liver slice of one rat is plotted in figure 3 and fitted by the nonlinear least squares fitting to a bi-exponential decay curve given by $S_p(t) = Ae^{-\alpha t} + Be^{-\beta t}$. The fitting parameters were A = 3,192 ± 128, α = 1.287 ± 0.051 min^{-1}, B = 2,232 ± 67, and β = 0.0932 ± 0.0056 min^{-1}. The Δ-signal time evolution of each tumor pixel was separated into the extravascular and intravascular components corresponding to the first and the second terms in equation [5] to extract the plasma volume fraction. Figure 4 shows a typical Δ-signal time course with the fitted extravascular and intravascular contributions. The fitting parameters were: v_p = 0.0203 ± 0.0020 ml/g, $K_{in}^{PS\rho}$ = 0.0589 ± 0.0041 min^{-1} and $K_{out}^{PS\rho}/v_e$ = 0.2440 ± 0.0146 min^{-1}. The plasma volume fraction was converted to the vascular volume fraction by multiplying with the factor 1/(1-Hct). Since the compartmental model is not applicable in regions of low perfusion the necrotic regions were excluded from the analysis.

For all the tumor pixels containing the perfluoro-15-crown-5-ether emulsion both pO_2 maps from F-19 images and the corresponding vascular volume fraction maps from the DCE-MRI were calculated. Then a histogram of pixels according to their vascular volume fraction (f_b) value was formed going from low to high f_b. Pixels falling within a range of Δf_b = 0.005 were averaged both in their f_b value as well as their corresponding pO_2 (F-19) values to improve the SNR. The process was repeated for all animals individually. The model constants C1, C2, and C3 were determined by fitting equations (3-4) to the experimental data. Figure 5 shows the measured pO_2 (F-19) using the F-19 images vs. the vascular volume fraction f_b obtained from the DCE-MRI for the corresponding regions. The error bars show the standard deviation in each measurement. The parameters obtained by least
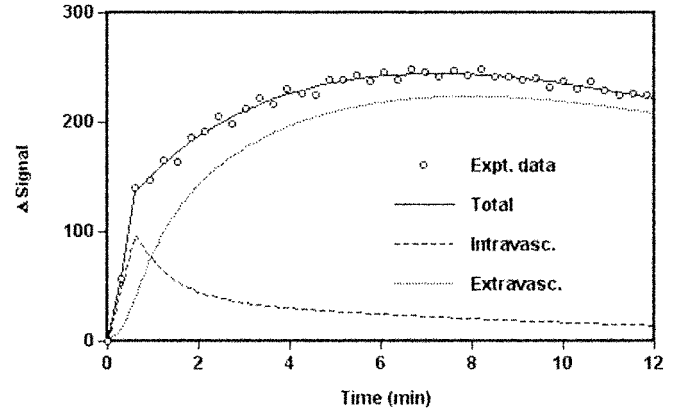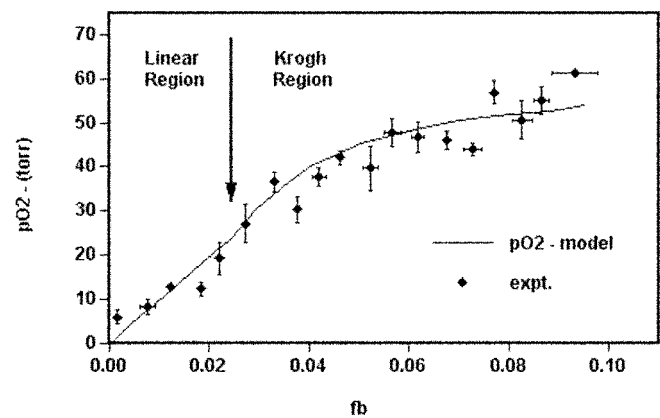

Figure 5: The (F-19) as a function of vascular volume fraction (f_b) measured in three rats was used for calibration. The solid curve is the extended Krogh model with the linear and non-linear regions as marked.

squares fitting of equations [3-4] to the experimental data were: C_1 = 983.2± 133.2 torr for f_b from 0 to 0.025; C_2 = 58.2 ± 2.4 torr, and C_3 = 1.7 ± 0.1 torr (r=0.88) for $f_b \geq 0.025$. The transition point, f_b = 0.025 where the two curves are tangent to each other, is also shown in the same figure.

Comparison of pO$_2$ values as Obtained from F-19 MRI and DCE-MRI

The performance of the extended Krogh model was then tested on two additional rats by performing both F-19 and DCE-MRI studies. The T$_2$ weighted anatomical images of these two rats, called Rat D and E, are shown in Figures 6a and 6b with the tumor region marked for each. We calculated the vascular volume fraction map for each animal as previously described. The vascular volume map of only the tumor region is shown Figures 6b and c for the same ani-
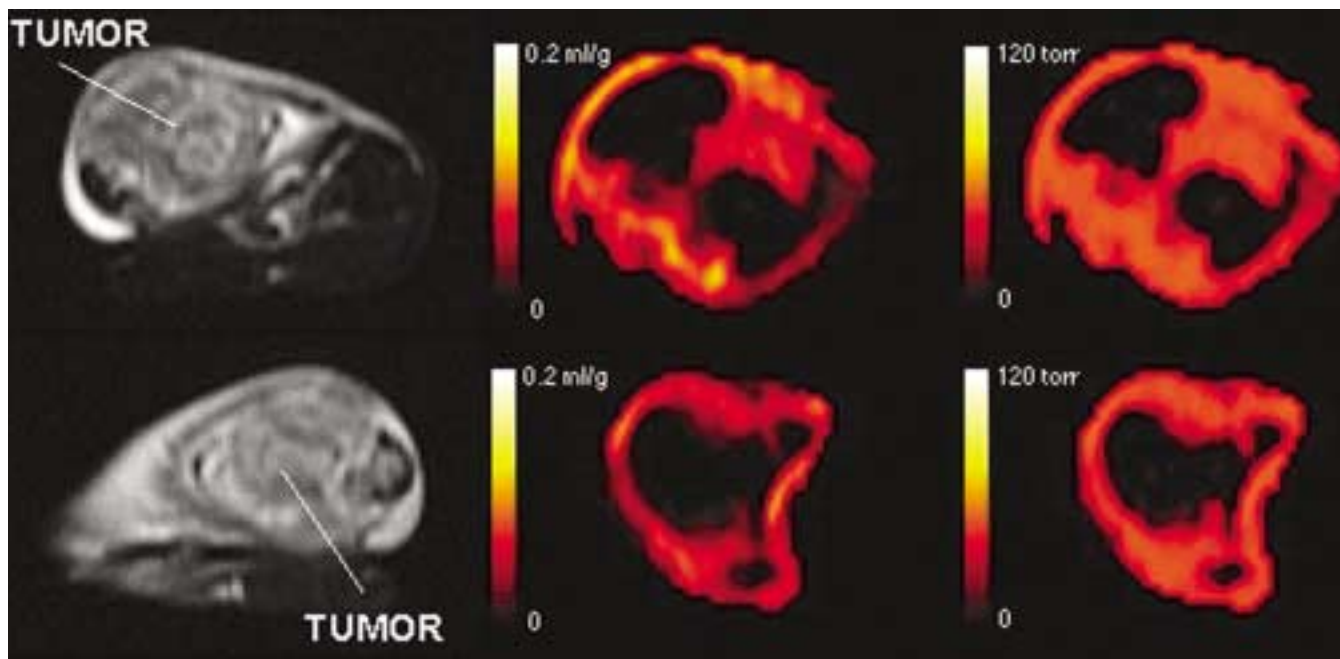
Figure 6: The T2 weighted anatomical images of the two rats used in testing the performance of the proposed technique are seen in the first column. Tumor regions are marked as shown. The vascular volume fraction maps obtained from the H-1 dynamic contrast enhanced MRI (second column) and the calculated oxygen tension maps (third column) are also shown in the same figure. Note that the calculated f_b and (H-1) maps only cover the tumor region where F-19 was localized. Furthermore, images given in the second and third column were magnified for better visualization. The top and bottom rows are for rats D and E, respectively.

mals. The vascular volume fraction at a given pixel was converted to the pO_2 (H-1) by using the extended Krogh model with the parameters and analysis method given in the previous subsection. The next figures, Figures 6c and 6f, show the calculated pO_2 (H-1) maps of the tumor on the same animals. Note that the f_b and pO_2 maps were magnified with respect to the anatomical images for better visualization. The calculated pO_2 (H-1)'s shown in Figures 6c and 6f were then compared with the pO_2 (F-19) obtained form the F-19 MRI study from the corresponding locations. The results obtained from two rats are shown in Figure 7. The figure also shows the linear regression line [pO_2 (H-1) = (1.01 $\pm$ 0.07) pO_2 (F-19) + (0.91 $\pm$ 0.05)]. It is seen that the measurements obtained by both techniques have a high degree of correlation r=0.96, supporting the applicability of the proposed model in determining pO_2 from the DCE-MRI study.

Discussion

Krogh's model for tissue oxygenation has been studied by many groups in the past (43-48). In this model, capillaries are assumed to be the only oxygen source, boundary conditions are assumed to be cylindrical, the oxygen distribution is assumed to be symmetric around the capillary, and no oxygen flux is assumed at the outer boundary of the Krogh's cylinder. Although quite simplistic, this approach still remains as one of the most significant models for describing tissue oxygenation and has been used extensively to calcu-

late tissue oxygen tension. In the present work, we extended it to calculate tumor oxygen tension from the vascular volume fraction as measured by the dynamic contrast enhanced MRI. The parameters of the model were determined from the tumor pixels that were measured by both F-19 MRI and the H-1 dynamic contrast enhanced MRI. We then tested the performance of this model on additional animals bearing Walker-256 tumors who also had both F-19 and DCE MRI. In taking this approach, we made the implicit assumption that the model's parameters remain constant for a given tumor type. Although this assumption could be a potential source of error, our results indicate the error to be insignificant as seen in Figure 7. We believe this is due to the fact that our technique produces an average value obtained from the whole tumor and the integrated blood oxygen tension averaged along the vessel wall surfaces, oxygen diffusion coefficient, solubility of oxygen in the tissue, capillary radius, and tissue metabolic consumption rate averaged over a large number of cells of the same type should remain relatively constant. For voxels containing large blood vessels, this approximation does not hold, but the oxygen tension in equation [3] saturates to the integrated blood oxygen tension when the vascular volume fraction increases. It should be noted that equation [3] derived from Krogh's model becomes singular when f_b approaches to zero. In order to extend the model to low pO_2 values, which are more interesting biologically, we further assumed that in this region the pO_2 is linearly proportional to f_b as given in equation [4]. This

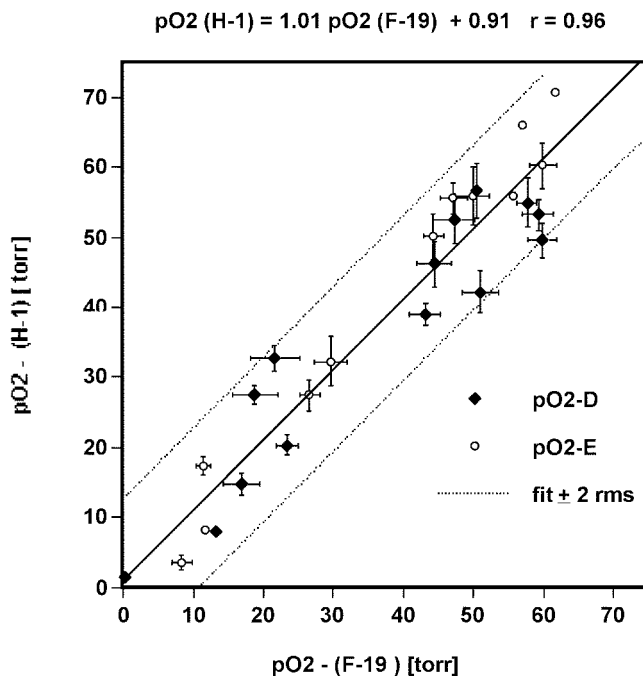**pO2 (H-1) = 1.01 pO2 (F-19) + 0.91   r = 0.96**

Figure 7: The calculated (H-1) vs. measured (F-19) for the two rats that were studied by both F-19 and H-1 MRI. The error bars show the standard deviation. Dotted lines show ± 2 x r.m.s. error of the fit.

assumption is valid when the oxygen diffusion from blood is the only source of the tissue oxygen supply. The oxygen diffusion distance is typically around 100 ☐m [55, 56], but the MRI voxel size is 1.25 mm x 1.25 mm x 5 mm, therefore the fraction of the oxygen diffused from other voxels should be small. The contribution gets even smaller when the voxel size gets larger.

Vaupel et al. (9, 57) studied the oxygenation of solid breast tumors with the oxygen electrode method. The median value of the breast tumor oxygen tension was 28 torr according to their measurements. The averaged oxygen tension we calculated from the dynamic contrast enhanced MRI for Walker 256 mammary carcinoma using five rats was 32.9 ± 6.7 torr, which is within the correct range.

Like most other perfluorocarbon emulsions, the relationship between the oxygen tension and the relaxation rate R1 of the perfluoro-15-crown-5-ether emulsion is also affected by the temperature. Dardzinski and Sotak (17) measured the temperature dependence of the perfluoro-15-crown-5-ether relaxation rates at 2.0 T. They determined that a one degree Celsius reduction in temperature can cause an increase of 0.013 sec^{-1} in the R_1, corresponding to an oxygen tension increase of 3.98 torr according to equations [2] and [4] in reference 21. This results in a 6.6% error in the pO_2 for pO_2 = 60 torr at 37 °C in a single pixel. The percentage error in pO_2 goes up to ~ 20% at 20 torr at 37 °C but can be reduced by averaging multiple pixels as was done in our investigation.

The relaxation rate calibration in our study was performed at 37 °C. In order to minimize errors arising from changes in the temperature we kept the body temperature at 37 °C by surrounding the animal in an insulating foam which was pre-heated to 37 °C by a lamp. The temperature of each animal was monitored throughout the experiment and was found to be 37.0 ± 1.0 °C averaged over five animals. Thus the error estimate for pO_2 due to changes in the temperature remained in the same range as discussed above. The mean oxygen tension was 32.9 ± 6.7 torr for all five Walker tumors studied here. Considering the fact that this is a pO_2 value averaged over all the pixels within a tumor and over five animals, the experimental error in pO_2 appears to be much larger than any errors that may arise from temperature changes when averaged over the same number of pixels. Therefore, we do not believe that temperature changes within ± 1 °C would contribute a significant amount of error to the measurement of pO_2 when compared to all the other experimental errors.

Dardzinski and Sotak (17) used the RIF-1 tumors, and determined the mean oxygen tension values to be 15 - 37 torr, which differed considerably among the individual tumors. One major difference between their study and ours is the fact that they injected the perfluoro-15-crown-5-ether emulsion intravenously and measured the oxygen tension of the sequestered PFC 3-7 days after the injection. We repeated this technique and observed no appreciable amount of PFC within the tumors while most of the PFC being sequestered in liver and spleen. The intratumoral PFC injection was first introduced by Mason et al (18). They measured tumor oxygen tension in Dunning prostate R3327-AT1 tumors by intratumorally injecting Hexafluorobenzene. The mean oxygen tension was determined to be 4.0 torr in the central region and 48.8 torr in the peripheral region. The Walker 256 tumors that were used in the present study had a tendency to develop necrosis in the central region; therefore we avoided this region when injecting the PFC emulsion. We also performed an experiment to monitor the amount of F-19 signal change in the tumor during the period it took to perform the oxygen tension measurement by repeating the spin echo pulse sequence with the same TR and TE values. The signal change was less than 4 % and no appreciable signal was detected in liver and spleen. Various H-1 MRI techniques have been investigated to study tumor oxygenation, such as the T_2* weighted signal [58, 59] and ADC (60). However, whether it is possible to relate T_2* or ADC is still an open question requiring further investigation.

In the present study, the fitted parameter C_2 related to the integrated blood oxygen tension was determined to be 58.2 torr which fell within the normal range between the venous and arterial oxygen tension. The second parameter C_3 value was 1.7 torr. This parameter is related in a complicated way to the oxygen diffusion coefficient, solubility of oxygen in

the tissue, capillary radius, and tissue metabolic consumption rate. In order to get a rough estimate, we assumed that the solubility of oxygen in tissue to be 9.4×10^{-10}, the oxygen diffusion coefficient is $1.75 \sim 3.04 \times 10^{-9}$ m^2/sec, the capillary radius is 5 mm, and the tissue metabolic consumption rate is 16 ml O_2/100gram•min (46, 61), then the calculated C3 value is $1.04 \sim 1.92$ torr from its definition. The values used for the oxygen diffusion coefficient, solubility of oxygen in the tissue, and tissue metabolic consumption rate in our estimation were from the muscle studies (46). Their values in a tumor could be somewhat different. However, the value obtained for the Walker-256 tumors was within the range obtained by estimation.

In the present investigation pixel wise tumor vascular volume fractions were obtained from the DCE MRI using the two-compartment model. This technique has been studied by several groups (29-37) and reviewed by Tofts (42). We used the general solution, equation [5], of the two-compartment model and replaced the contrast concentrations in equation [5] by the Δ-signals. By doing this, we assumed that the Δ-signal is linearly proportional to the contrast concentration and the constant of proportionality is independent of the material. The linearity is a valid assumption under the condition of short TR, and the constant of proportionality depends on the proton density and is independent of T_{10}, as shown by Tofts (42). The proton density could slightly depend on the type of the tissue, but as a first approximation it can be assumed to be the same for various tissues. We also assumed that the Gd-DTPA kinetics in the liver is similar to that of blood (62). The signal time course that was measured from the liver showed a typical bi-exponential decay of the blood Gd-DTPA contrast agent kinetics (63) with a fast decay constant of 1.287 ± 0.051 min^{-1} and a slow decay constant of 0.0932 ± 0.0056 min^{-1}. These decay constants are close to the ones that were obtained from the blood Gd-DTPA concentration as reported by Wedeking et al (64). As assumed in the work by others on compartmental modeling analysis, the constant of proportionality between the Gd-DTPA concentration and its induced relaxation rate change $D(1/T_1)$ is approximately the same for various types of tissues, which has been confirmed by various measurements (65-67).

Conclusions

We developed an extended model based on the Krogh's cylindrical model to calculate tumor oxygen tension from the H-1 dynamic contrast enhanced MRI. The parameters of the model were determined by performing sequential F-19 MRI oxygen tension measurement and the dynamic Gd-DTPA enhanced MRI on the same tumor slices. Tumor vascular volume fractions were derived from a compartmental modeling analysis of the dynamic contrast enhanced MRI time

series, and tumor oxygen tension maps were calculated from the vascular volume fractions for Walker 256 tumors implanted in rats. We found that model parameters determined using three rats was accurate to calculate the in two additional rats bearing the same type of tumor. The measurements done by H-1 MRI had an excellent correlation (r=0.96) with the pO_2's measured by F-19 MRI from the same locations. Thus, the current study supports the feasibility of oxygen tension mapping by H-1 dynamic contrast enhanced MRI using proper modeling and analysis. In spite of some of the limitations that were mentioned earlier, our work extends Krogh's model to the low range and also illustrates how dynamic contrast enhanced MRI might be useful in monitoring tumor in a practical manner.

References and Footnotes

1. Gray, L. H., Conger, A.D., Ebert, M., Hornsey, S., Scott, O.C.A., The concentration of oxygen dissolved in tissues at the time of irradiation as a factor in radiotherapy. *Br. J. Radiol. 26*, 628-654 (1953).
2. Hill, R.P. and Pallavicini, M.G., Hypoxia and the radiation response of tumors. *Adv. Exp. Med. Biol. 159*, 17-35 (1983).
3. Kallman, R.F., and Dorie, M.J., Tumor oxygenation and reoxygenation during radiation therapy: their importance in predicting tumor response. *Int. J. Radiat. Oncol. Biol. Phys. 12*, 681-685 (1986).
4. Okunieff, P., Hoeckel, M., Dunphy, E.P., Schlenger, K., Knoop, C., and Vaupel, P., Oxygen tension distributions are sufficient to explain the local response of human breast tumors treated with radiation alone. *Int. J. Radiat. Oncol. Biol. Phys. 26*, 631-636 (1993).
5. Hall, E.J., Radiobiology for the radiologist, 4th edition, Philadelphia, J. B. Lippincott Company, pp. 133-151 (1994).
6. Cater, D.B. and Silver, I.A., Quantitative measurements of oxygenation in normal tissues and in the tumors of patients before and after radiotherapy. *Acta Radiol. 53*, 233-256 (1960).
7. Hockel, M., Schlenger, K., Knoop, C., and Vaupel, P., Oxygenation of carcinomas of the uterine cervix: evaluation by computerized O$_2$ tension measurement. *Cancer Res. 51*, 6098-6102 (1991).
8. Lartigau, E., Le Ridant, A-M., Lambin, P., Weeger, P., Martin, L., Sigal, R., Lusinchi, A., Luboinski, B., Eschwege, F., and Guichard, M., Oxygenation of head and neck tumors. *Cancer 71*, 2319-2325 (1993).
9. Vaupel, P., Schlenger, K., Knoop, C., and Hockel, M., Oxygenation of human tumors: evaluation of tissue oxygen distribution in breast cancers by computerized O$_2$ tension measurements. *Cancer Res. 51*, 3316-3322 (1991).
10. Goldacre, R.J., and Sylven, B., On the access of blood-borne dyes to various tumor regions. *Br. J. Cancer 16*, 306-322 (1962).
11. Song, C.W., and Levitt, S.H., Quantitative study of vascularity in Walker carcinoma 256. *Cancer Res. 31*, 587-589 (1971).
12. Le, D., Mason, R.P., Hunjan, S., Constantinescu, A., Barker, B.R.,

and Antich, P.P., Regional tumor oxygen dynamics: [19]F PBSR EPI of hexafluorobenzene. *Magn. Reson. Imag. 15*, 971-981 (1997).

13. Baldwin, N.J. and Ng, T.C., Oxygenation and metabolic status of KHT tumors as measured simultaneously by ^{19}F magnetic resonance imaging and ^{31}P magnetic resonance spectroscopy. *Magn. Reson. Imag. 14*, 514-551 (1996).

14. Guo, Q., Mattrey, R.F., Guclu, C., Buxton, R.B., and Nalcioglu, O., Monitoring of pO$_2$ by spin-spin relaxation rate $1/T_2$ of ^{19}F in a rabbit abscess model. Artificial Cells, *Blood Substitutes, and Immobilization Biotechnology, 22*, 1449-1454 (1994).

15. Hees, P.S., and Sotak, C.H., Assessment of changes in murine tumor oxygenation in response to nicotinamide using ^{19}F NMR relaxometry of a perfluorocarbon emulsion. *Magn. Reson. Med. 29*, 303-310 (1993).

16. R. P. Mason, P. P. Antich, E. E. Bobcock, A. Constantinescu, P. Peschke, and E. W. Hahn, Non-invasive determination of tumor oxygen tension and local variation with growth. *Int. J. Radiat. Oncol. Biol. Phys. 29*, 95-103 (1994).

17. Dardzinski, B.J., and Sotak, C.H., Rapid tissue oxygen tension mapping using ^{19}F inversion-recovery echo-planar imaging of perfluoro-15-crown-5-ether. *Magn. Reson. Med. 32*, 88-97 (1994).

18. Mason, R.P., Rodbumrung, W., and Antich, P.P., Hexafluorobenzene: a sensitive ^{19}F NMR indicator of tumor oxygenation. *NMR. Biomed. 9*, 125-134 (1996).

19. Jao, J-C., and Nalcioglu, O., Measurement of pO2 by spatially localized double-voxel F-19 imaging and spectroscopy of PFB. *Physica Medica XI*, 121-126 (1995).

20. Fishman, J.E., Joseph, P.M., Floyd, T.F., Mukherji, B., and Sloviter, H.A., Oxygen-sensitive ^{19}F NMR imaging of the vascular system in vivo. *Magn. Reson. Imag. 5*, 279-285 (1987).

21. Mason, R.P., Antich, P.P., Babcock, E.E., Gerberich, J.L., and Nunnally, R.L., Perfluorocarbon imaging in vivo: a ^{19}F MRI study in tumor-bearing mice. *Magn. Reson. Imag. 7*, 475-485 (1989).

22. Ozdemirel, B., and Nalcioglu, O., Correction of chemical-shift artifacts in multislice F-19 imaging with perfluorooctyl bromide. *Magn. Reson. Med. 23*, 324-332 (1992).

23. Lee, H.K., and Nalcioglu, O., Reblurred deconvolution method for chemical shift removal in F-19 (PFOB) MR imaging. *J. Magn. Reson. Imag. 2*, 53-61 (1992).

24. Lee, H.K., and Nalcioglu, O., Reduced-bandwidth method for F-19 imaging of perflubron. *J. Magn. Reson. Imag. 2*, 563-568 (1992).

25. Lee, H.K., Nalcioglu, O., and Buxton, R.B., Correction of chemical-shift artifacts in ^{19}F imaging of PFOB: a robust signed magnitude method. *Magn. Reson. Med. 23*, 254-263 (1992).

26. Mason, R.P., Shukla, H., and Antich, P.P., In vivo oxygen tension and temperature: simultaneous determination using ^{19}F NMR spectroscopy of perfluorocarbon. *Magn. Reson. Med. 29*, 296-302 (1993).

27. Sotak, C.H., Hees, P.S., Huang, H.N., Hung, M.H., Krespan, C.G., and Raynolds, S., A new perfluorocarbon for use in fluorine-19 magnetic resonance imaging and spectroscopy. *Magn. Reson. Med. 29*, 188-195 (1993).

28. Holland, S.K., Kennan, R.P., Schaub, M.M., D'Angelo M.J., and Gore, J.C., Imaging oxygen tension in liver and spleen by 19F NMR. *Magn. Reson. Med. 29*, 446-458 (1993).

29. McGovern, K.A., Schoeniger, J.S., Wehrle, J.P., Ng, C.E., and Glickson, J.D., Gel-entrapment of perfluorocarbons: a fluorine-19 NMR spectroscopic method for monitoring oxygen concentration in cell perfusion systems. *Magn. Reson. Med. 29*, 196-204 (1993).

30. Noth, U., Morrissey, S.P., Deichmann, R., Adolf, H., Schwarzbauer, C., Lutz, J., and Haase, A., In vivo measurement of partial oxygen pressure in large vessels and in the reticuloendothelial system using fast ^{19}F-MRI. *Magn. Reson. Med. 34*, 738-745 (1995).

31. Harms, S.E., Flaming, D.P., Hesley, K.L., and Evans, W.P., Magnetic resonance imaging of the breast. *Magn. Reson. Quarterly 8*, 139-155 (1992).

32. Flicinger, F.W., Allison, J.D., Sherry, R.M., and Wright, J.C., Differentiation of benign from malignant breast masses by time-intensity evaluation of contrast enhanced MRI. *Magn. Reson. Imag. 11*, 617-620 (1993).

33. Mussurakis, S., Buckley, D.L., Bowsley, S.J., Carleton, P.J., Fox,, J.N. Turnbull, L.W., and Horsman, A., Dynamic contrast-enhanced magnetic resonance imaging of the breast combined with pharmco-kinetic analysis of gadolinium-DTPA uptake in the diagnosis of local recurrence of early stage breast carcinomna. *Investive Radiology 30*, 650-662 (1995).

34. Larsson, H.B., Stubgaard, M., Frederiksen, J.L., Jensen., M., Henriksen, O., and Paulson, O.B., Quantitation of blood-brain barrier defect by magnetic resonance imaging and gadolinium-DTPA in patients with multiple sclerosis and brain tumors. *Magn. Reson. Med. 16*, 117-131 (1990).

35. Tofts, P.S. and Kermode, A., Measurement of the blood-brain barrier permeability and leakage space using dynamic MR imaging. 1. Fundamental concepts. *Magn. Reson. Med. 17*, 357-367 (1991).

36. Brix, G., Semmler, Port, W.R., Schad, L.R., Layer, G., and Lorenz,, W.J. Pharmacokinetic parameters in CNS Gd-DTPA enhanced MR imaging. *J. Comput. Assist. Tomogr. 15*, 621-628 (1991).

37. Gowland, P., Mansfield, P., Bullock, P., Stehling, M., Worthington, B., and Firth, J., Dynamic studies of gadolinium uptake in brain tumors using inversion-recovery echo planar imaging. *Magn. Reson. Med. 26*, 241-258 (1992).

38. Kenney, J., Schmiedl, U., Maravilla, K., Starr, F., Graham, M., Spence, A., and Nelson, J., Measurement of blood-brain barrier permeability in a tumor model using magnetic resonance imaging with gadolinium-DTPA. *Magn. Reson. Med. 27*, 68-75 (1992).

39. Su, M-Y., Jao, J-C., and Nalcioglu, O., Measurement of vascular volume fraction and blood-tissue permeability constants with a pharmacokinetic model: studies in rat muscle tumors with dynamic Gd-DTPA enhanced MRI. *Magn. Reson. Med. 32*, 714-724 (1994) .

40. Su, M-Y., Najafi, A.A., and Nalcioglu, O., Regional comparison of tumor vascularity and permeability parameters measured by albumin-Gd-DTPA and Gd-DTPA. *Magn. Reson. Med. 34*, 402-411 (1995).

41. Tofts, P.S., Berkowitz, B., and Schnall, M.D., Quantitative analysis of dynamic Gd-DTPA enhancement in breast tumors using a permeability model. *Magn. Reson. Med. 33*, 564-568 (1995).

42. Tofts, P.S., Modeling tracer kinetics in dynamic Gd-DTPA MR imaging. *J. Magn. Reson. Imag. 7*, 91-101 (1997).

43. Krogh, A., The number and distribution of capillaries in muscle with the calculation of oxygen pressure necessary for supplying the tissue. *J. Physiol. 52*, 409-515 (1918).

44. Hyman, W.A., A simplified model of the oxygen supply function of capillary blood flow. *Adv. Exp. Med. Biol. 37B*, 835-838 (1973).

45. Piiper, J., and Scheid, P., Cross-sectional PO$_2$ distributions in Krogh cylinder and solid cylinder models. *Respir. Physiol. 64*, 241-251 (1986).

46. Groebe, K., and Thews, G., Role of geometry and anisotropic diffusion for modeling PO$_2$ profiles in working red muscle. *Respir. Physiol. 79*, 255-278 (1990).

47. Groebe, K., and Thews, G., Basic mechanisms of diffusive and diffusion-related oxygen transport in biological systems: a review. *Adv. Exp. Med. Biol. 317*, 21-33 (1992).

48. Intaglietta, M., Johnson, P.C., and Winslow, R.M., Microvascular and tissue oxygen distribution. *Cardiovas. Res. 32*, 632-643 (1996).

49. Fine, D.L., Arthur, L.O., and Young, L.J., Cell culture factors influencing in vitro expression of mouse mammary tumor virus. *In Vitro 12*, 693-701 (1976).

50. Parhami, P., and Fung, B.M., Fluorine-19 relaxation study of perflu-

oro chemicals as oxygen carriers. *J. Phys. Chem. 87*, 1928-1931 (1983).

51. Kuwatsuru, R., Shames, D.M., Muhler, A., Mintorovitch, J., Vexler, V., Mann, J.S., Cohn, F., Price, D., J. Huberty, J., and Brasch, R.C., Quantification of tissue plasma volume in the rat by contrast-enhanced magnetic resonance imaging. *Magn. Reson. Med. 30*, 76-81 (1993).

52. Shames, D.M., Kuwatsuru, R., Vexler, V.S., Muhler, A., and Brasch, R.C., Measurement of capillary permeability to macromolecules by dynamic magnetic resonance imaging: a quantitative noninvasive technique. *Magn. Reson. Med. 29*, 616-622 (1993).

53. Schwickert, H.C., Roberts, T.P., DShames, D.M., van Dijke, C.F., Disston, A., Muhler, A., Mann, J.S., and Brasch R.C., Quantification of liver blood volume: comparison of ultra short TI inversion recovery echo planar imaging (ULSTIR-EPI), with dynamic 3D-gradient recalled echo imaging. *Magn. Reson. Med. 34*, 845-852 (1995).

54. Demsar, F., Roberts, T.P., Schwickert, H., Shames, D.M., van Dijke, C.F., Mann, J.S., Saeed, M., and Brasch, R.C., A MRI spatial mapping technique for microvascular permeability and tissue blood volume based on macromolecular contrast agent distribution. *Magn. Reson. Med. 37*, 236-42 (1997).

55. Thomlinson, R.H. and Gray, L.H., The histological structure of some human lung cancer and the possible implications for radiotherapy. *Br. J. Cancer 9*, 539-549 (1955).

56. Brown, J.M., Tumor hypoxia, drug resistance, and Metastases. *J. Natl. Cancer. Inst. 82*, 338-339 (1990).

57. Vaupel, P., Schlenger, K., and Hoeckel, M., Blood flow and tissue oxygenation of human tumors: an update. *Adv. Exp. Med. Biol. 317*, 139-151 (1992).

58. Karczmar, G.S., Kuperman, V.Y., River, J.N., Lewis, M.Z., and Lipton, M.J., Magnetic resonance measurement of response to hyperoxia differentiates tumors from normal tissue and may be sensitive to oxygen consumption. *Investigative Radiology 29*, S161-S163 (1994).

59. Howe, F.A., Robinson, S.P., and Griffiths, J.R., Modification of tumour perfusion and oxygenation monitored by gradient recalled echo MRI and ^{31}P MRS. *NMR Biomed. 9*, 208-216 (1996).

60. Dunn, J.F., Ding, S., O'Hara, J.A., Liu, K.J., Rhodes, E., Weaver, J.B., and Swartz, H.M., The apparent diffusion constant measured by MRI correlates with pO_2 in a RIF-1 tumor. *Magn. Reson. Med. 34*, 515-519 (1995).

61. Less, J.R., Skalak, T.C., Sevick, E.M., and Jain, R.K., Microvascular architecture in a mammary carcinoma: branching patterns and vessel dimensions. *Cancer Res. 51*, 265-273 (1991).

62. Su, M-Y., Wang, Z., Roth, G.M., Lao, X., Samoszuk, M.K., and Nalcioglu, O., Pharmacokinetic changes induced by vasomodulators in kidneys, livers, muscles, and implanted tumors in rats as measured by dynamic Gd-DTPA-enhanced MRI. *Magn. Reson. Med. 36*, 868-877 (1996).

63. Weinmann, H.J., Laniado, M., and Mutzel, W., Pharmacokinetics of GdDTPA/dimeglumine after intravenous injection into healthy volunteers. *Physiol. Chem. Phys. Med. NMR 16*, 167-172 (1984).

64. Wedeking, P., Eaton, S., Covell, D.G., Nair, S., Tweedle, M.F., Eckelman, W.C., Pharmacokinetic analysis of blood distribution of intravenously administered [153]Gd-labeled $Gd(DTPA)_2$- and [99mTc](DTPA) in rats. *Magn. Reson. Imag. 8*, 567-575 (1990).

65. Braunschweiger, P.G., Schiffer, L.M., and Furmanski, P., 1H-NMR relaxation times and water compartmentalization in experimental tumor models. *Magn. Reson. Imag. 4*, 335-342 (1986).

66. Donahue, K.M., Burstein, D., Manning, W.J., and Gray, M.L., Studies of Gd-DTPA relaxivity and proton exchange rates in tissue. *Magn. Reson. Med. 32*, 66-76 (1994).

67. Shuter, B., Tofts, P.S., Wang, S.C., and Pope, J.M., The relaxivity of Gd-EOB-DTPA and Gd-DTPA in liver and kidney of the Wistar rat. *Magn. Reson. Imag. 14*, 243-253 (1996).